Available online at www.sciencedirect.com
ScienceDirect
Journal of Photochemistry and Photobiology A: Chemistry 190 (2007) 177–189
Journal of Photochemistry and Photobiology A:Chemistry
www.elsevier.com/locate/jphotochem

Photoinduced multi-mode quantum dynamics of pyrrole at the $^1\pi\sigma^*$– S_0 conical intersections

Zhenggang Lan [a,*], Arnaud Dupays [a], Valérie Vallet [b], Susanta Mahapatra [c], Wolfgang Domcke [a,*]

[a] *Department of Chemistry, Technical University of Munich, D-85747 Garching, Germany*
[b] *Laboratoire PhLAM, UMR CNRS 8523, Université des Sciences et Technologies de Lille, 59655 Villeneuve Dáscq Cedex, France*
[c] *School of Chemistry, University of Hyderabad, Hyderabad 500046, India*

Available online 21 January 2007

Abstract

The photoinduced dynamics of pyrrole at the $^1A_2(\pi\sigma^*)$– S_0 and $^1B_1(\pi\sigma^*)$– S_0 conical intersections has been investigated by multi-mode time-dependent quantum wave-packet calculations. Diabatic potential-energy surfaces have been constructed for both conical intersection using accurate multi-reference *ab initio* electronic-structure calculations. In addition to the NH stretching coordinate, the three (four) symmetry-allowed coupling modes of A_2 (B_1) symmetry have been considered for the $^1A_2(\pi\sigma^*)$– S_0 ($B_1(\pi\sigma^*)$– S_0) conical intersections. Wave-packet dynamics calculations have been performed for three-dimensional models, taking account of the two dominant coupling modes of each conical intersection. The electronic population-transfer processes at the conical intersections, the branching ratio for the dissociation to the ground and excited states of the pyrrolyl radical, and their dependence on the initial preparation of the system have been investigated. It is shown that the excitation of the NH stretching mode strongly enhances the photodissociation rate, while the excitation of the strongest coupling mode has a pronounced effect on the branching ratio of the photodissociation process. Although the inclusion of the second (weaker) coupling mode has little effect on the electronic population dynamics, it leads to interesting changes of the nodal pattern of the wave packet at the conical intersections. The calculations provide insight into the effect of the multiple coupling modes on the process of direct photodissociation through a conical intersection.

Keywords: Photodissociation of pyrrole; Photochemistry of pyrrole; $\pi\sigma^*$ state; Conical intersections; Wavepacket

1. Introduction

Ab initio calculations have revealed that the near-UV photolysis of pyrrole essentially involves the four lowest excited singlet states, which are $^1A_2(\pi\sigma^*)$, $^1B_1(\pi\sigma^*)$, $^1B_2(\pi\pi^*)$, and $^1A_1(\pi\pi^*)$ [1–5] (see Fig. 1). The ordering of the vertical excitation energies of these four states has been quite controversial [1–3]. The two $^1\pi\pi^*$ states are responsible for the broad and intense absorption band near 6 eV. The two lowest excited singlet states are of $^1\pi\sigma^*$character. At the ground-state equilibrium geometry, the σ^* orbital is essentially a 3s Rydberg orbital. Upon stretching of the NH bond, the potential-energy (PE) functions of the $^1\pi\sigma^*$ states are repulsive. They intersect the PE function of the electronic ground state, resulting in the $^1A_2(\pi\sigma^*)$– S_0 and $^1B_1(\pi\sigma^*)$– S_0 conical intersections [4] (see Fig. 1). These conical intersections provide a mechanism for ultrafast internal conversion (that is, radiationless decay to the electronic ground state), as well as hydrogen abstraction [4]. The latter process has been confirmed by the experimental detection of fast hydrogen atoms in the photodissociation of pyrrole [6–9].

The nonadiabatic photoinduced dynamics of pyrrole has been investigated via time-dependent quantum wave-packet calculations on two-dimensional *ab initio* PE surfaces [10,11]. The NH stretching mode has been considered as well as the dominant coupling mode at the $^1A_2(\pi\sigma^*)$– S_0 and $^1B_1(\pi\sigma^*)$– S_0 conical intersections, respectively [11]. The model calculations in reduced dimensionality have revealed two key features: (1) the time scale of the hydrogen abstraction is extremely sensitive to the initial vibrational level of the NH stretching mode, and (2) the branching ratio for photodissociation into the $^2\pi$ and $^2\sigma$ pyrrolyl radicals depends on the initial excitation of the cou-

* Corresponding authors. Tel.: +49 89 28913609.
E-mail addresses: lan@ch.tum.de (Z. Lan), domcke@ch.tum.de (W. Domcke).

1010-6030/$ – see front matter © 2007 Elsevier B.V. All rights reserved.
doi:10.1016/j.jphotochem.2007.01.018

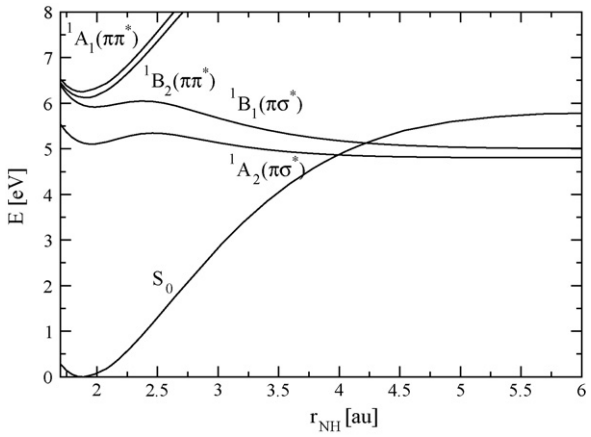

Fig. 1. Potential energy of the five lowest singlet electronic states, S_0, $\pi\sigma^*$ ($^1A_2$), $\pi\sigma^*$ ($^1B_1$), $\pi\pi^*$ ($^1B_2$) and $\pi\pi^*$ ($^1A_1$) of pyrrole as functions of r_{NH}.

pling mode [11]. The conical intersections between the $^1\pi\pi^*$ and $^1\pi\sigma^*$ states have been characterized in Ref. [12].

Very recently, Ashfold and co-workers have applied high-resolution photofragment translational spectroscopy at several excitation wave lengths to pyrrole and several other heteroaromatic molecules [13–16]. These experiments have revealed that the pyrrolyl radical (as well as the corresponding radicals of other heteroaromatics) is formed in remarkably limited subsets of its available state density. Such mode-specific product formation after photoexcitation of medium-size organic molecules would have been considered, until recently, very unusual. Such vibrational mode-specific photodissociation dynamics is now recognized as a signature of ultrafast nonadiabatic dynamics via conical intersections [16].

In the present work, we have extended the previous calculations [10,11] by investigating the effect of all symmetry-allowed coupling modes [17] for each $^1\pi\sigma^*$– S_0 conical intersection in pyrrole. We treat the two $^1\pi\sigma^*$– S_0 conical intersections separately. We construct models of reduced dimensionality to explore the quantum nonadiabatic dynamics at the individual conical intersections. Multi-reference electronic-structure methods have been employed to characterize the coupling modes. Few-dimensional PE surfaces have been constructed on the basis of these *ab initio* data, following the strategy of previous works [10,11]. The essential features of the ultrafast hydrogen-abstraction dynamics of photoexcited pyrrole are explored, employing standard quantum wave-packet (WP) propagation methods.

2. Theory

2.1. Ab initio calculation of the adiabatic PE surfaces

In our calculations, we have used the augmented correlation-consistent polarised-valence-double-zeta (aug-cc-pVDZ) basis set [18]. To properly describe the Rydberg character of the $^1\pi\sigma^*$ states in the Frank-Condon (FC) region, one additional diffuse *s* function and one additional set of *p* functions were added at the nitrogen atom, as well as two additional diffuse *s* and two additional sets of diffuse *p* functions at the active hydrogen atom. Their exponents were derived by dividing successively the exponent of the most diffuse *s* and *p* functions in the aug-cc-pVDZ basis by factor of 3.0.

The ground-state equilibrium geometry, the normal modes and the harmonic vibrational frequencies of pyrrole have been obtained with the second-order Møller-Plesset (MP2) method using the GAUSSIAN 98 package [19].

To characterise the $^1A_2$– S_0 and $^1B_1$– S_0 conical intersections, we have performed two independent *ab initio* complete-active-space self-consistent-field (CASSCF) calculations by averaging the CASSCF functional over the $^1A_2$ and S_0, and the $^1B_1$ and S_0 states, respectively. These calculations were performed with the MOLPRO package [20].

For the calculation of the $^1A_2$– S_0 conical intersection, the active space consists of three π orbitals and two π^* orbitals, as well as one occupied σ orbital and the corresponding σ^* orbital of Rydberg character. This active space corresponds to a distribution of 8 electrons in 7 orbitals. For the calculation of the $^1B_1$– S_0 conical intersection, besides the orbitals included in the $^1A_2$– S_0 calculation, it was found to be necessary to include two additional occupied orbitals of σ character ($8a_1$, $6b_2$), and three additional virtual orbitals of σ^* character ($11a_1 - 12a_1$, $7b_2$) to obtain smooth PE surfaces in the region of the barrier of the $^1B_1$ ($\pi\sigma^*$) surface, where the $^1\pi\sigma^*$ state changes its character from 3s towards H1s. Thus, the active space is composed of 12 electrons in 12 orbitals. As pointed out in a recent study by Celani and Werner [5], this active space yields the correct ordering of the low-lying valence and Rydberg states of interest.

2.2. Analytic representation of the diabatic PE surfaces

The *ab initio* calculations yield the adiabatic PE surfaces. The adiabatic representation is not convenient for the treatment of the reaction dynamics due to the singularity of derivative couplings at the conical intersection [21]. Thus, we introduce a so-called quasi-diabatic electronic representation via a suitable unitary transformation of the electronic states [21–23].

The diabatic-to-adiabatic transformation matrix $\mathbf{U}$ of the electronic wavefunctions is generally defined as

$$\mathbf{\Phi}^{a} = \mathbf{U}\mathbf{\Phi}^{d}, \tag{1}$$

where $\mathbf{\Phi}^{a}$ and $\mathbf{\Phi}^{d}$ are two-dimensional vectors of adiabatic and diabatic electronic wave functions, respectively. The adiabatic PE matrix $\mathbf{V}^{a}$ is obtained from the diabatic PE matrix $\mathbf{V}^{d}$ via

$$\mathbf{V}^{a} = \mathbf{U}\mathbf{V}^{d}\mathbf{U}^{+}. \tag{2}$$

The diagonal elements of the matrix $\mathbf{V}^{d}$ are the diabatic PEs correlating with the S_0 and one of the two $^1\pi\sigma^*$ states, respectively. The off-diagonal element of $\mathbf{V}^{d}$ represents the electronic couplings between different diabatic states.

In the present rather transparent case of a single conical intersection, arising from the symmetry-allowed crossing of one of the $^1\pi\sigma^*$ states and the S_0 state, we can achieve the diabatization via the *ansatz* of a 2 × 2 diabatic PE matrix as an analytic func-

tion of the nuclear coordinates. The parameters of the *ansatz* are determined by a least-squares fit of the eigenvalues of the PE matrix to the *ab initio* PE data. The details of the diabatic models can be found in Appendix A.

2.3. Multi-mode Hamiltonian

The Hamiltonian for nuclear motion is expressed in the two-state diabatic basis as

$$H = T_{\mathrm{N}} \begin{pmatrix} 1 & 0 \\ 0 & 1 \end{pmatrix} + \begin{pmatrix} V_{11} & V_{12} \\ V_{21} & V_{22} \end{pmatrix}. \tag{3}$$

where T_{N} is the nuclear kinetic-energy operator. V_{11} and V_{22} describe the PE surfaces of the ground diabatic S_0 state and the diabatic $^1\pi\sigma^*$ state, respectively.

The selection of the relevant modes of the reduced dimensionality models can be performed with the help of symmetry selection rules. Since pyrrole possesses $C_{2\mathrm{v}}$ symmetry, its 24 internal degrees of freedom correspond to nine A_1, three A_2, eight B_1 and four B_2 vibrational modes:

$$\Gamma = 9\Gamma_{\mathrm{A}_1} + 3\Gamma_{\mathrm{A}_2} + 8\Gamma_{\mathrm{B}_1} + 4\Gamma_{\mathrm{B}_2}. \tag{4}$$

The NH stretching coordinate r_{NH} of A_1 symmetry is the reaction coordinate for the hydrogen abstraction reaction. For the $^1A_2$– S_0 conical intersection, the coupling coordinates [17] are the three normal coordinates of A_2 symmetry. For the $^1B_1$–S_0 conical intersection, the coupling coordinates are the four normal coordinates of B_1 symmetry. These selection rules result in models which include four or five degrees of freedom for the $^1A_2$– S_0 or $^1B_1$– S_0 conical intersections, respectively.

In this set of coordinates, the kinetic-energy operator takes the following form:

$$T_{\mathrm{N}} = -\frac{\hbar^2}{2\mu}\frac{\partial^2}{\partial r^2} - \sum_c \frac{1}{2}\omega_c \frac{\partial^2}{\partial Q_c^2}, \tag{5}$$

where μ is the reduced mass corresponding to the motion of the H atom relative to the ring part of pyrrole. r is defined as the distance between the H atom and the center of mass of the ring. Q_c are dimensionless normal coordinates with corresponding frequencies ω_c. Here the summation is over all symmetry-allowed coupling modes.

In the present rather simplified model, all other internal coordinates are kept frozen at their ground-state equilibrium values. This means that we ignore the energy transfer between the active modes and the many other vibrational modes. It should be mentioned that we also ignore here the possible coupling between the $^1B_1(\pi\sigma^*)$ and $^1A_2(\pi\sigma^*)$ states via in-plane vibrational modes of B_2 symmetry [24,25]. Moreover, we do not consider the vibronic interaction of the $^1\pi\sigma^*$ states with the optically allowed $^1\pi\pi^*$ states via out-of-plane modes [12]. The experimental results of Ashfold's group have revealed that these vibronic inducing modes are spectator modes, that is, their quantum states do not change during the photodissociation process [14,16].

2.4. Effective-mode Hamiltonian

The concept of effective tuning and coupling modes has been discussed in previous works (see Refs. [17,26–28] and the references therein). It has been shown that the effective mode is a good approximation when the tuning (coupling) modes possess similar frequencies [17,26,27].

In the case of a conical intersection with several coupling modes with frequencies ω_c and coupling strength λ_c, a single mode, the so-called effective coupling mode, can be constructed to represent the effects of all coupling modes. The coupling strength λ_{eff} and the frequency Ω_{eff} of this effective coupling mode are [17,26,27]

$$\lambda_{\mathrm{eff}} = \sqrt{\sum_c \lambda_c^2}, \tag{6}$$

$$\Omega_{\mathrm{eff}} = \sum_c \frac{\lambda_c}{\lambda_{\mathrm{eff}}}\omega_c, \tag{7}$$

$$Q_{\mathrm{eff}} = \sum_c \frac{\lambda_c}{\lambda_{\mathrm{eff}}} Q_c. \tag{8}$$

This approximation reduces the dimensions of our models from four ($^1A_2$–S_0 intersection) or five ($^1B_1$–S_0 intersection) to two: the NH stretching mode and the effective coupling mode.

2.5. Preparation of the initial states, WP propagation and population probabilities

The vibrational eigenstates of the adiabatic ground-state PE surface are constructed within the time-independent framework, by the diagonalization of the adiabatic ground-state Hamiltonian in a finite-basis representation. The initial WPs are prepared by vertical electronic excitation, that is, by placing a given vibrational state of the electronic ground state into one of the $^1\pi\sigma^*$ excited states. The photoinduced dynamics of pyrrole is treated in the time-dependent picture by solving the time-dependent Schrödinger equation for the nuclear motion on the coupled surfaces in the diabatic representation. For the large-amplitude NH stretching coordinate, we adopt the representation of the WP on an equidistant grid. For the coupling modes, it is more economical to employ an expansion of the WP in harmonic-oscillator basis functions. The details of this mixed-grid-basis representation (MGBR) are explained in Appendix B.

Adiabatic and diabatic electronic population probabilities are defined as expectation values of the corresponding projection operators, $|\phi^{\mathrm{a}}\rangle\langle\phi^{\mathrm{a}}|$ or $|\phi^{\mathrm{d}}\rangle\langle\phi^{\mathrm{d}}|$, with the time-dependent vibronic wave function [17]

$$P_i^{\mathrm{d}}(t) = \langle\Psi(t)|\phi_i^{\mathrm{d}}\rangle\langle\phi_i^{\mathrm{d}}|\Psi(t)\rangle, \quad i = 1, 0, \tag{9}$$

$$P_i^{\mathrm{a}}(t) = \langle\Psi(t)|\phi_i^{\mathrm{a}}\rangle\langle\phi_i^{\mathrm{a}}|\Psi(t)\rangle, \quad i = 1, 0. \tag{10}$$

For the present dissociative system, we use a special trick to calculate the diabatic and adiabatic populations. The details can be found in Appendix C.

Table 1
Harmonic vibrational frequencies of the ground state of pyrrole obtained with the MP2 methods

Mode	Symmetry	ω (cm^{-1})	
		MP2	DFT
ν_1	A_1	3672.8	3674.7
ν_2	A_1	3304.8	3262.2
ν_3	A_1	3283.2	3240.0
ν_4	A_1	1494.7	1500.5
ν_5	A_1	1430.7	1417.1
ν_6	A_1	1167.5	1173.8
ν_7	A_1	1096.0	1092.2
ν_8	A_1	1035.9	1033.8
ν_9	A_1	882.0	901.9
ν_{10}	A_2	824.3	878.2
ν_{11}	A_2	664.9	686.9
ν_{12}	A_2	608.8	631.0
ν_{13}	B_2	3298.5	3256.3
ν_{14}	B_2	3271.9	3228.7
ν_{15}	B_2	1544.9	1576.5
ν_{16}	B_2	1480.7	1455.8
ν_{17}	B_2	1291.3	1309.0
ν_{18}	B_2	1156.7	1159.0
ν_{19}	B_2	1056.0	1066.6
ν_{20}	B_2	858.9	881.3
ν_{21}	B_1	792.6	830.9
ν_{22}	B_1	716.2	727.8
ν_{23}	B_1	637.1	641.0
ν_{24}	B_1	515.9	474.9

The frequencies obtained with the DFT method and the B3LYP functional (Ref. [13]) are given for comparison.

3. Results and discussion

3.1. Ab initio results

The calculated equilibrium geometry of the ground state of pyrrole is in good agreement with previous results [1–3,5,29–31]. The normal modes, their symmetry labels and the harmonic vibrational frequencies are given in Table 1 for the convenience of the reader. The vibrational frequencies are in good agreement with previous theoretical data (see Ref. [13] and references therein). The atomic displacement vectors associated with the normal modes of A_2 and B_1 symmetry are shown in Fig. 2.

For the $^1A_2$– S_0 conical intersection, the vibronic coupling constants λ_c of the three A_2 modes at the conical intersection are given in Table 2. The mode ν_{11} is found to be the strongest coupling mode with a dimensionless coupling parameter $\lambda/\omega =$ 1.34. The other two modes, ν_{10} and ν_{12}, are rather weak coupling modes, with dimensionless coupling parameters in the range 0.42 − 0.46, three times smaller than that of mode ν_{11}.

Table 2
Harmonic vibrational frequencies ω, $^1A_2$– S_0 coupling parameter λ and dimensionless coupling parameter λ/ω of three A_2 modes at the $^1A_2$– S_0 conical intersection

Mode	ω (eV)	λ (eV)	λ/ω
ν_{10}	0.102	0.043	0.422
ν_{11}	0.083	0.111	1.337
ν_{12}	0.075	0.035	0.467

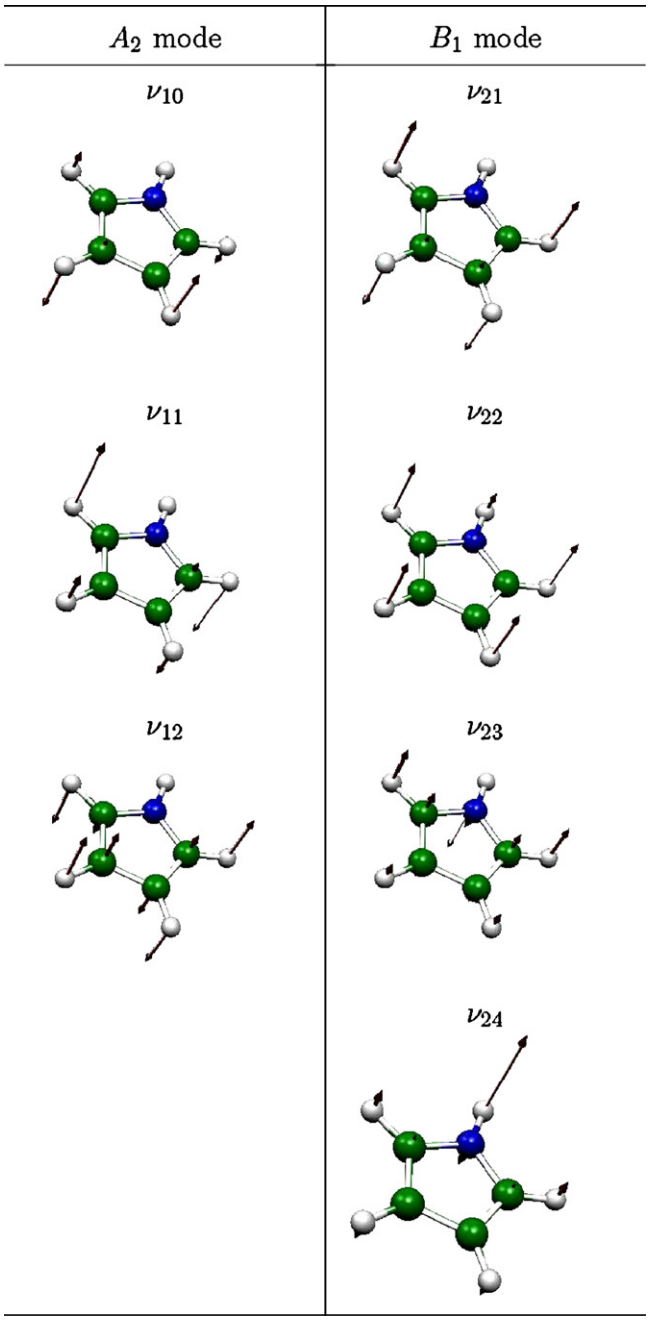

Fig. 2. Nuclear displacement vectors of the A_2 and B_1 normal modes of pyrrole.

For the $^1B_1$– S_0 conical intersection, the coupling constants of the four B_1 modes at the conical intersection are given in Table 3. Among them, the strongest coupling mode is ν_{24} with the dimensionless coupling parameter 5.53. This mode possesses the lowest frequency and mainly represents the out-of-plane motion of the H atom of the azine group (see Fig. 2). The mode ν_{22} is also a relevant coupling mode, with $\lambda/\omega \sim 0.8$. It corresponds to a combination of the out-of-plane motion of the H atom of the azine group and similar motions of the H atoms of the ring (see Fig. 2). The modes ν_{21} and ν_{23}, representing the

Table 3
Harmonic vibrational frequencies ω, $^1B_1$– S_0 coupling parameter λ and dimensionless coupling parameter λ/ω of the four B_2 modes at the $^1B_1$– S_0 conical intersection

Mode	ω (eV)	λ (eV)	λ/ω
ν_{21}	0.098	0.0	0.0
ν_{22}	0.089	0.072	0.809
ν_{23}	0.079	0.0	0.0
ν_{24}	0.064	0.354	5.531

out-of-plane motions of the N atom or H atoms of the ring, are essentially inactive (see Table 3).

3.2. $^1A_2$– S_0 conical intersection

The coupling strength of ν_{11} is much stronger than that of the other two modes of A_2 symmetry. In the previous work, we have taken just this coordinate into account as the coupling coordinate to construct a two-dimensional (2D) model [11]. The coupling modes ν_{10} and ν_{12} have similar coupling strengths at the conical intersection and their coupling strengths are much weaker than that of ν_{11}. To investigate their effect on the dynamics of the $^1A_2$– S_0 conical intersection, we can add either of them to the 2D model to obtain a three-dimensional (3D) model. We have performed WP calculations by adding either the mode ν_{10} or ν_{12}. The results show that the influence of ν_{12} on the dynamics is more prominent than that of ν_{10}. Therefore, we discuss only the results of the 3D model which includes the strong coupling mode ν_{11} and the weak coupling mode ν_{12}.

3.2.1. Vibrational eigenstates of the electronic ground-state surface

The lowest vibrational levels of the 3D electronic ground-state surface of the $^1A_2$– S_0 conical intersection model have been calculated by diagonalization of the ground state Hamiltonian. We designate the occupation numbers of the NH stretching mode, the strong coupling mode (ν_{11}) and the weak coupling mode (ν_{12}) as n_r, $n_{c,1}$ and $n_{c,2}$, respectively. The fundamental frequencies of these three vibrations are 3405, 675 and 613 cm^{-1}, respectively, in the 3D model, in acceptable agreement with the experimental and full-dimensional harmonic frequencies (see [31,32] and references therein).

3.2.2. Electronic population and WP dynamics

As discussed previously for the 2D model of the $^1A_2$–S_0 conical intersection, the photodissociation rates are highly dependent on the preparation of the initial state of the NH stretching mode. When the NH stretching mode is prepared in its ground state [$(0, n_{c,1}, n_{c,2})$ initial condition], no fast dynamics takes place due to the presence of a rather high barrier in the $^1A_2$ ($\pi\sigma^*$) state (0.40 eV). The energies of the initial states are significantly lower than this barrier. The WP is therefore trapped in the well of the $^1A_2$ state. It can escape only by quantum tunnelling, which happens on a rather long time-scale. In addition, the top of the barrier on the $^1A_2$ ($\pi\sigma^*$) surface is lower in energy than the upper adiabatic dissociation limit ($^2\sigma$). The upper dissociation channel is therefore closed and the WP dissociates towards the lower limit ($^2\pi$).

If we put one quantum of energy into the NH stretching motion [$(1, n_{c,1}, n_{c,2})$ initial condition], the adiabatic population probabilities exhibit extensive population transfer within 20 fs (see Fig. 3). In this case, the WP can overcome the barrier in the $^1A_2$ state and reach the conical intersection very quickly due to the strongly repulsive character of the $^1A_2$ surface. At the conical intersection, the WP splits and moves towards both dissociation channels, $^2\pi$ and $^2\sigma$. Since the top of the barrier in the $^1A_2$ state is slightly lower than the upper ($^2\sigma$) dissociation limit, only the high-energy part of the WP can dissociate towards the upper dissociation limit directly. The low-energy part of the WP (with an energy between the barrier of the $^1A_2$ state and the upper dissociation limit), is reflected by the attractive upper adiabatic potential and re-enters the conical intersection. This part of the WP oscillates at the conical intersection, and finally dissociates to the ground state of the pyrrolyl radical. This explains the decay of the diabatic population of the $^1A_2$ state in the early stage of the reaction and the recovery of it in the later stage. When two quanta of the NH stretching mode are initially excited [$(2, n_{c,1}, n_{c,2})$ initial condition], we also observe very fast decays of the P_1^a populations (not shown here). However, the enhancement of the decay time relative to $n_r = 1$ is not significant. The recovery of the diabatic population P_2^d disappears in this case.

For the above cases, all of the wave packet moves to the two dissociation channels and the the total photodissociation probability is unity in the present treatment. It is interesting to notice that the branching ratio of the reaction is sensitive to the preparation of the dominant coupling mode ν_{11}. The diabatic population transfer at the conical intersection is enhanced by the excitation of this mode (see Fig. 3). On the other hand, the excitation of the weak coupling mode ν_{12} has almost no effect on the population dynamics (see Fig. 3). This result shows that the nonadiabatic transition at the conical intersection is primarily driven by the mode ν_{11}.

It is worthwhile to compare these results with our previous calculations including only the strong coupling mode ν_{11}. The inclusion of the additional coupling mode ν_{12} has a minor effect on the electronic population dynamics. This result confirms the validity of the original 2D model for the $^1A_2$– S_0 conical intersection [11].

3.2.3. Comparison of 2D and 3D WP dynamics

Although the 2D and 3D calculations predict a similar electronic population dynamics for the $^1A_2$–S_0 conical intersection, the comparison of details of the WP dynamics can provide additional insight into the multi-mode dynamics at this conical intersection. For the sake of illustration, we analyze the evolution of the WP for the initial preparation in the (1,0) vibrational state in the 2D model and compare it with the WP dynamics for the (1,0,0) initial preparation in the 3D model. The probability densities of the 2D WP are displayed as the absolute squares of the projection of the nuclear WP on the diabatic $^1A_2$ and S_0 states. For the 3D case, we define reduced probability densities for two vibrational modes by integration of the absolute square

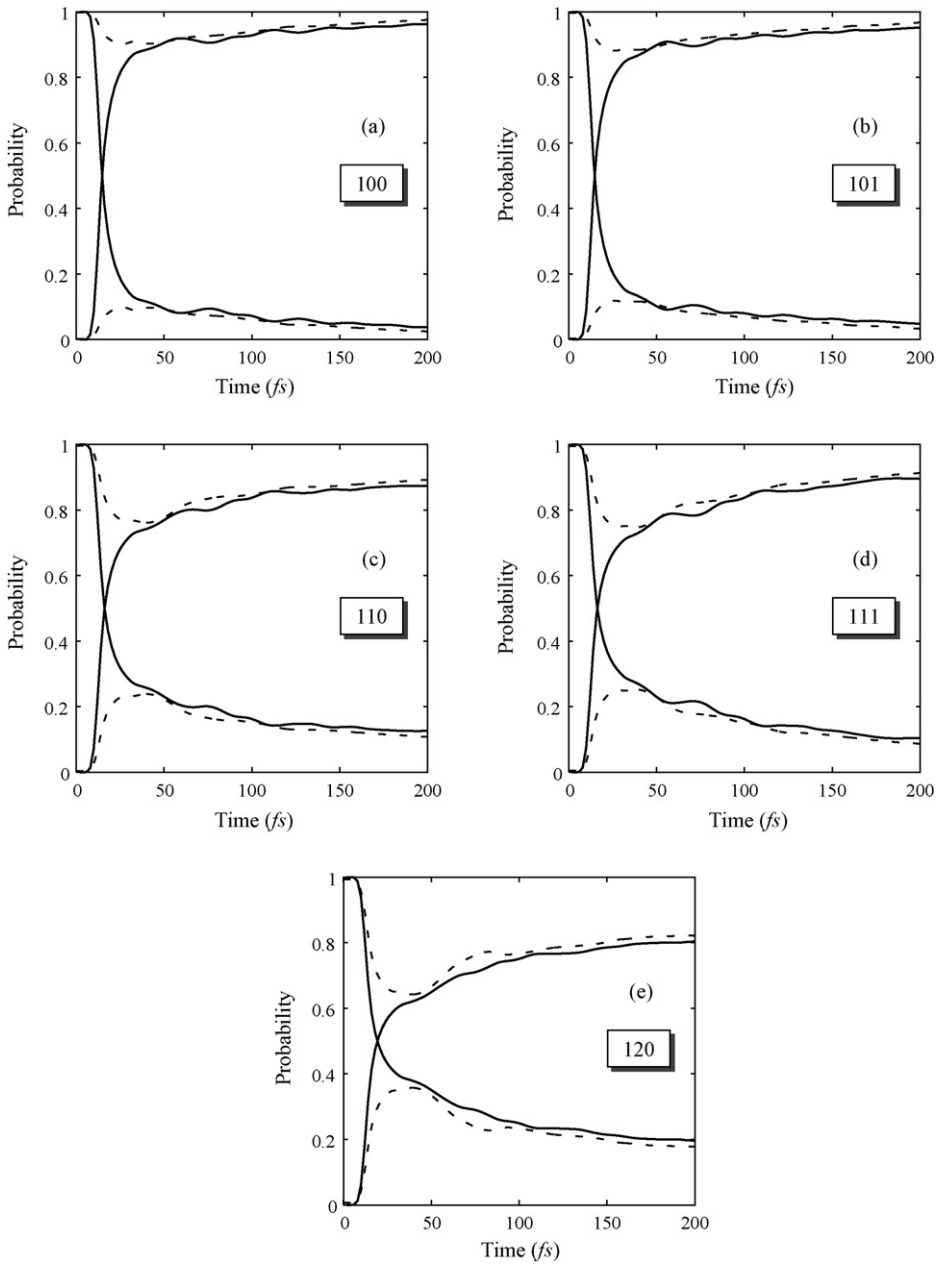

Fig. 3. Time-dependent diabatic (dashed lines) and adiabatic (full lines) population probabilities of the $^1A_2$ and S_0 states for the initial states (1 0 0) (a), (1 0 1) (b), (1 1 0) (c), (1 1 1) (d), (1 2 0) (e).

of the nuclear WP over the third vibrational mode. The snapshots are taken at 20 fs after the preparation of the excited state.

Fig. 4(a and b) shows the probability densities as functions of r and Q_{11} for the diabatic $^1A_2$ and S_0 states, respectively, for the 2D model. The WP, which has been prepared in the $^1A_2$ state at $t = 0$ fs, has arrived at the conical intersection at 20 fs. The central part of the WP remains in the $^1A_2$ state, while the wing parts have preferentially been transferred to the S_0 state. Since the excitation of the coupling mode increases the extension of the WP along Q_{11}, the WP for $n_{c,1} > 0$ tends to follow the adiabatic surfaces rather than the diabatic surfaces. This explains the influence of the excitation of the coupling mode on the electronic population dynamics, which is clearly seen in Fig. 3. When the WP is transferred to the diabatic S_0 state, a nodal line is created at $Q_{11} = 0$ by the $^1A_2$– S_0 conical intersection (see Fig. 4(b)). This reflects the fact that the diabatic coupling operator is an odd function of the coupling coordinate.

Fig. 4(c and d) shows the corresponding probability densities for the 3D model, as functions of r and Q_{11}. For the WP in the excited state, there is no obvious difference between the 2D and 3D results (Fig. 4(a and c)), except that the 3D calculation yields a somewhat broader distribution of the probability density along the coupling coordinate. The snapshot of the WP in the ground state (Fig. 4(b and d)), on the other hand, reveals a remarkable difference between the 2D and 3D calculations. In the 3D calculation, the reduced probability density at $Q_{11} = 0$ is not zero.

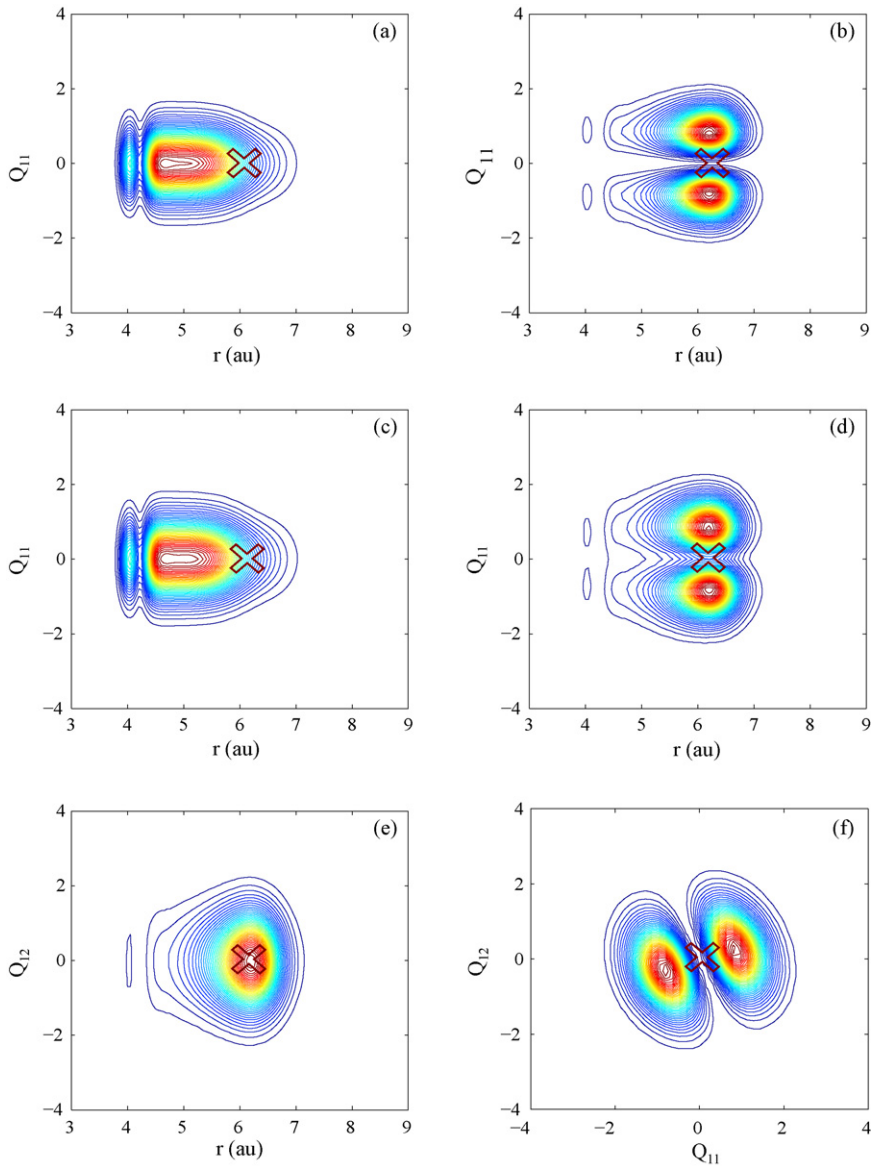

Fig. 4. Snapshots of the probability density as a function of the NH stretching mode and one of the coupling modes at 20 fs: (a) probability density as a function of r and Q_{11} of the $^1A_2$ state obtained for the 2D model; (b) probability density as a function of r and Q_{11} in the S_0 state obtained for the 2D model; (c) probability density as a function of r and Q_{11} in the diabatic $^1A_2$ state obtained for the 3D model; (d) probability density as a function of r and Q_{11} for the diabatic S_0 state obtained for the 3D model; (e) probability density as a function of r and Q_{12} in the diabatic S_0 state obtained for the 3D model; (f) probability density as a function of Q_{11} and Q_{12} in the diabatic S_0 state obtained for the 3D model.

The inclusion of the weak coupling mode thus modifies the symmetry properties of the WP as a function of the strong coupling mode.

In the adiabatic representation, the nonadiabatic coupling vector, which induces the nonadiabatic transition, is parallel to the direction of effective coupling mode displacement Q_{eff} [26] (see Eq. (6)). In the diabatic representation, Q_{eff}, which is a linear combination of all Q_c, determines the population transfer between the two surfaces. This means that the projection of the WP on the effective coupling coordinate exhibits a node structure of the WP like in the 2D case. In the present example, Q_{11} is the strong coupling coordinate, while the coupling of Q_{12} is rather weak. Q_{eff} therefore is quite close to Q_{11}, but the small contribution of Q_{12} leads to a deviation of the orientation of Q_{eff} from Q_{11}. This explains the blurring of the nodal structure of the probability density in Fig. 4(d). As a complementary result, we show in Fig. 4(e) the probability density in the diabatic ground state as a function of r and Q_{12} (the weak coupling mode). The density of Fig. 4(e) is totally different from that of Fig. 4(d) and exhibits no node at all. Finally, Fig. 4(f) shows the probability density in the diabatic ground state as a function of Q_{11} and Q_{12}. This figure exhibits the nodal line in the WP perpendicular to the effective coupling mode.

3.3. $^1B_1$– S_0 *conical intersection*

Since the coupling strength of ν_{21} and ν_{23} is negligible, it suffices to consider the strong coupling mode ν_{24} and the weak

coupling mode ν_{22}, resulting in a 3D model for the $^1B_1$– S_0 conical intersection. Since our previous 2D calculations [11] were based on a slightly different definition of the coupling mode, it is not useful to compare the present 3D results with the earlier 2D results. We have repeated the 2D calculations, including the NH stretching motion and the strong coupling mode ν_{24}.

3.3.1. Vibrational eigenstates of the electronic ground-state surface

The lowest vibrational levels of the 3D electronic ground-state surface of the $^1B_2$– S_0 conical intersection model have been calculated in the same way as for the $^1A_2$– S_0 model. Again, n_r, $n_{c,1}$ and $n_{c,2}$ denote the occupation numbers of the NH stretching mode, the strongest coupling mode (ν_{24}) and the weak coupling mode (ν_{22}), respectively. The fundamental frequencies of these three vibrational motions are 3616, 471 and 623 cm^{-1}, respectively, in the 3D model, in acceptable agreement with the experimental and full-dimensional harmonic values (see [31,32] and references therein).

3.3.2. Electronic population and WP dynamics

The decay rate of the population of the $^1\pi\sigma^*$ state is again strongly dependent on the initial excitation of the NH stretching mode. Other than in the $^1A_2$– S_0 case, we observe two processes with distinctly different time-scales when the NH stretching mode is prepared in its ground state [(0, $n_{c,1}$, $n_{c,2}$) initial con-

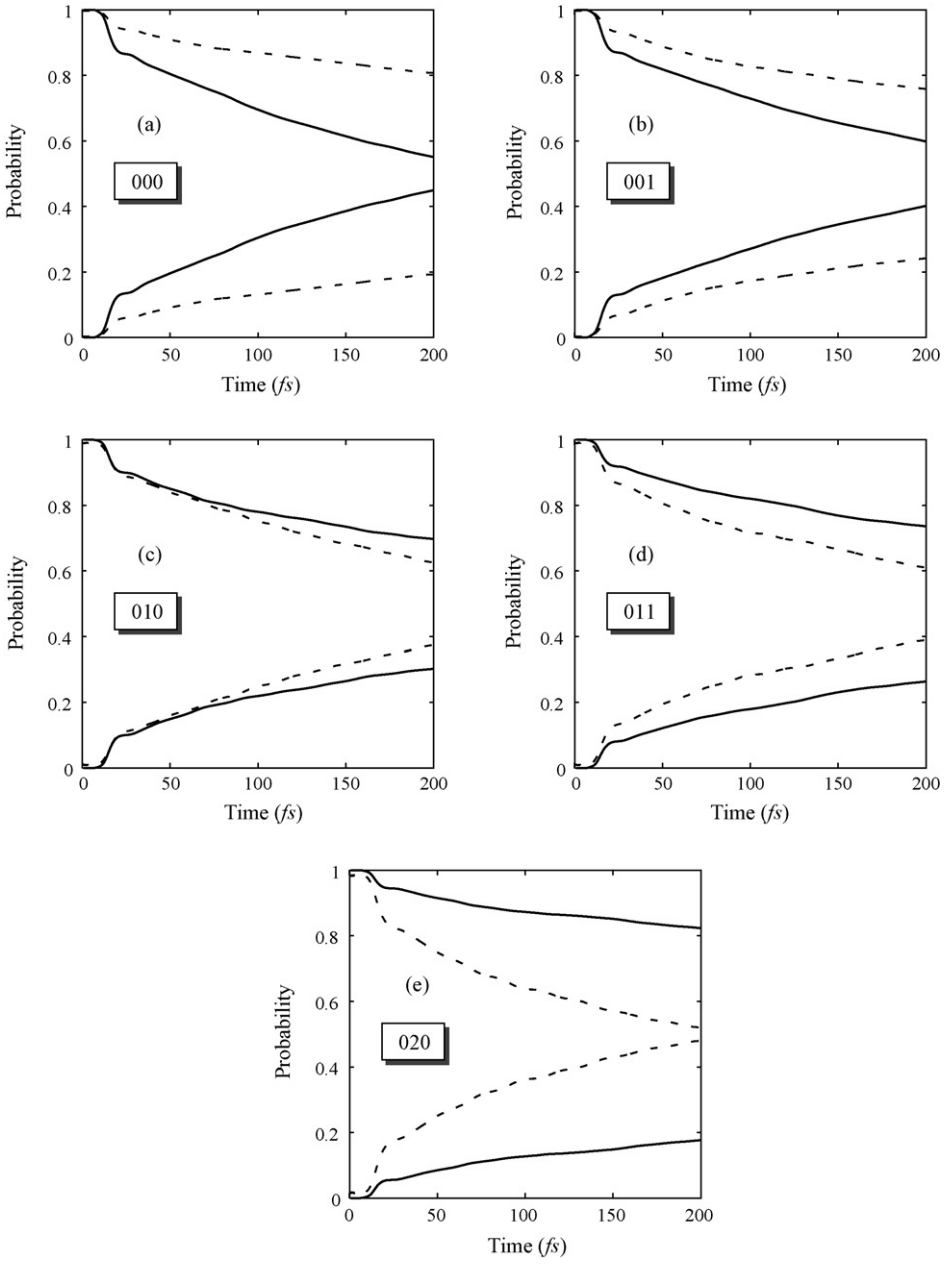

Fig. 5. Diabatic (dashed lines) and adiabatic (full lines) population probabilities of the $^1B_1$ and S_0 states for the initial states (0 0 0) (a), (0 0 1) (b), (0 1 0) (c), (0 1 1) (d), (0 2 0) (e).

dition]. Both the diabatic and adiabatic pictures indicate a rapid population transfer from the excited state to the ground state during the early stage of the dynamics (about 15 fs), followed by a slow and monotonic decay (see Fig. 5). This dynamics can be understood as follows. The barrier in the NH-stretching PE function is lower in the $^1B_1(\pi\sigma^*)$ state than in the $^1A_2(\pi\sigma^*)$ state (see Fig. 1). The high-energy component of the WP in the $^1B_1$ state therefore can overcome the barrier and can reach the conical intersection quickly, resulting in the fast initial decay. The low-energy part, on the other hand, can reach the conical intersection only by quantum tunnelling, resulting in the subsequent slow decay. When the NH stretching mode is initially excited, that is for the $(1, n_{c,1}, n_{c,2})$ (Fig. 6) and $(2, n_{c,1}, n_{c,2})$ (not shown here) initial conditions, the WP reaches the conical intersection within 15 fs and the population transfer is essentially completed after 25 fs. In these cases, the initial WP has sufficient energy to overcome the barrier, reach the conical intersection and move towards to the two dissociation limits directly.

Figs. 5 and 6 show the electronic dynamics of the 3D $^1B_1$–S_0 conical-intersection model for various initial conditions. The initial vibrational state of the strong coupling mode (ν_{24}) has a large effect on the branching ration of the reaction (see Figs. 5 and 6). Let us consider the $(1, n_{c,1},0)$ initial condition as a typical example. The excitation of the strong coupling mode enhances the probability of the adiabatic pathway from 30% for $n_{c,1} = 0$ to almost 50% for $n_{c,1} = 1$. The branching ratio saturates at about

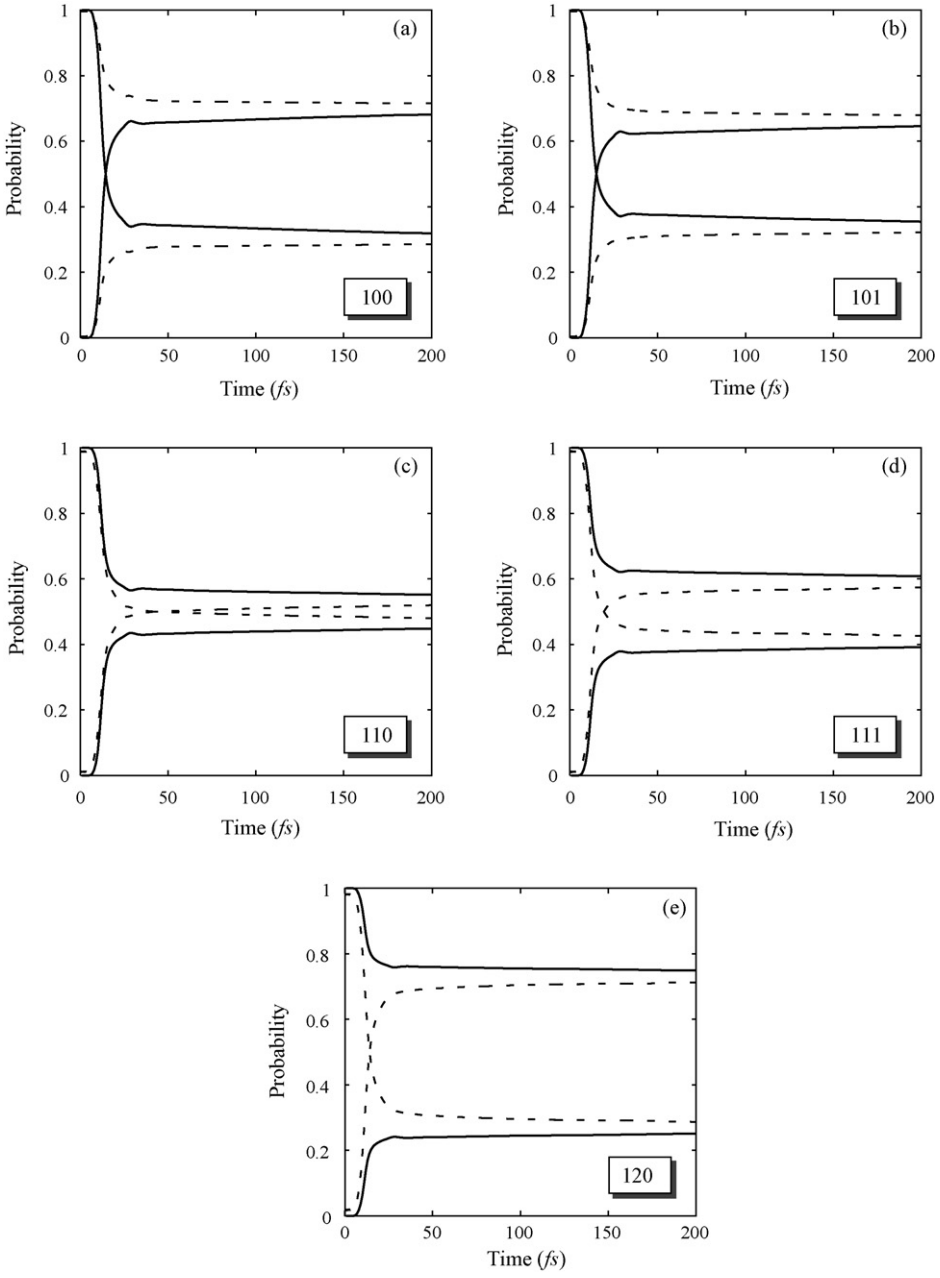

Fig. 6. Diabatic (dashed lines) and adiabatic (full lines) population probabilities of the $^1B_1$ and S_0 states for the initial states (1 0 0) (a), (1 0 1) (b), (1 1 0) (c), (1 1 1) (d), (1 2 0) (e).

70% for $n_{c,1} = 2$. The excitation of the weak coupling mode, on the other hand, has a rather small effect on the population dynamics. The probability of the adiabatic channel increases by about 5% for the excitation of one quantum of ν_{22}.

As a result of the weak effect of ν_{22} on the nonadiabatic transition at the conical intersection, the calculations based on the 2D, 3D and effective-mode models provide rather similar population dynamics. These results can can be analyzed in the same manner as discussed above by considering the orientation of Q_{eff}. Therefore, we do not repeat the detailed discussion of the probability densities here.

4. Conclusions

In order to understand the effect of additional vibrational modes on the $^1\pi\sigma^*$ driven photochemistry of pyrrole, we have investigated the nonadiabatic dynamics of the $^1B_1$– S_0 and $^1A_2$– S_0 coupled electronic states. For both of these conical intersections, we have determined the coupling strengths of all symmetry-allowed coupling modes. We have constructed 3D models which include the reaction coordinate (the NH stretching motion), one strong coupling mode, as well as one weak coupling mode.

The adiabatic PE surfaces have been computed with the CASSCF method. The ultrafast dynamics of the 3D conical-intersection models has been investigated using standard time-dependent quantum WP propagation methods. We have investigated the effects of the preparation of different initial vibrational states on the nonadiabatic dynamics.

The timescale of the photochemistry of pyrrole is extremely sensitive to the preparation of the initial state of the NH stretching mode. The excitation of the NH stretching mode strongly enhances the rate of decay of the excited electronic state. This acceleration of the nonradiative decay rate saturates at $n_r = 1$.

The 3D calculations reveal that for both conical intersections the nonadiabatic dynamics is governed by the strongest coupling mode to a good approximation. Although the weak coupling mode leads to interesting changes of the nodal pattern of the WP at the conical intersection, it has little effect on the electronic population dynamics. This confirms that the previously developed two-mode models of the $^1A_2$– S_0 and $^1B_1$– S_0 conical intersections are quite useful for the qualitative understanding of the mechanisms of the photoinduced dynamics of pyrrole. Both of the 2D and 3D models predict that the excitation of the strong coupling mode has a pronounced effect on the branching ratio of the photodissociation products. It should be therefore be possible to control the photodissociation dynamics of pyrrole via the combination of IR and UV excitations, as has been demonstrated for ammonia recently [33,34].

The extension of the theoretical description of the photodissociation dynamics of pyrrole should include the $^1B_2$ ($\pi\pi^*$) and $^1A_1$ ($\pi\pi^*$) states, which are primarily populated when pyrrole is excited with wavelengths shorter than 220 nm. A more comprehensive description of the photodissociation process thus involves five electronic states [S_0, $^1A_2$ ($\pi\sigma^*$), $^1B_1$ ($\pi\sigma^*$), $^1B_2$ ($\pi\pi^*$), and $^1A_1$ ($\pi\pi^*$)] and several types of conical intersections, $\pi\pi^*$– $\pi\sigma^*$ [12], $\pi\sigma^*$– S_0 [10,11], as well as $\pi\pi^*$– S_0 [35]. Although each of these conical intersections has been characterized individually, a comprehensive picture of the dynamics of the photodissociation process has yet to be developed. It is known, for example, that the $^2A_2$ and $^2B_1$ electronic states of the pyrrolyl radical are strongly coupled through a conical intersection [24,25] involving in-plane modes of B_2 symmetry. The photodissociation via the upper ($^1B_1$) $\pi\sigma^*$ state of pyrrole thus occurs in competition with the $^2B_1$– $^2A_2$ radiationless decay process in the pyrrolyl fragment.

In the present few-dimensional models of pyrrole, the quantum yield for photodissociation is unity, since the large excess energy of the NH stretching mode cannot be absorbed by the other degrees of freedom. In a full-dimensional description, the system can be stabilized by rapid intramolecular energy transfer from the active modes of the $^1\pi\sigma^*$– S_0 conical intersections to the remaining normal modes, resulting in internal conversion to the electronic ground state in competition with photodissociation. The quantum dynamical treatment of these processes represents a challenge for future theoretical work.

Acknowledgments

This work has been supported by the Deutsche Forschungsgemeinschaft and the Fonds der Chemischen Industrie. The authors wish to thank the Leibniz Rechenzentrum der Bayerischen Akademie der Wissenschaften for providing an ample amount of computer time. A.D. and V.V. acknowledge support by an Alexander von Humboldt research fellowship. V.V. also thanks the Centre d'Études et de Recherches Lasers et Applications, which is supported by Ministère Chargé de la Recherche, Région Nord/Pas-de-Calais and the Fonds Européen de Développement Économique des Régions (FEDER).

Appendix A. The diabatic models

In this appendix, we describe the extension of the previously developed 2D models (NH stretching coordinate and one coupling mode) by including all symmetry-allowed coupling modes (three for the $^1A_2$– S_0 conical intersection and four for the $^1B_1$– S_0 conical intersection).

In the multi-mode models for the $^1A_2$– S_0 and $^1B_1$– S_0 conical intersections, the diabatic S_0 PE surface is modelled by a Morse function for the tuning coordinate r_{NH} and harmonic functions of the coupling coordinates Q_c

$$V_{11} = v_{11}(r_{\text{NH}}) + \sum_c \frac{1}{2}\omega_c^{(1)}(r_{\text{NH}})Q_c^2, \tag{A.1}$$

with

$$v_{11}(r_{\text{NH}}) = D_e^1[1 - \exp(-a_1(r_{\text{NH}} - r_1))]^2, \tag{A.2}$$

where r_1 corresponds to the equilibrium NH distance of the diabatic S_0 state and D_e^1 is the dissociation energy.

The PE functions of the $^1\pi\sigma^*$ states display a barrier along the NH stretch coordinate. To describe this barrier, we employ an avoided-crossing model, combining a Morse potential (v_{21}, for the bound part) and a repulsive exponential potential (v_{22}, for

the dissociation region). The diabatic potential functions of the coupling modes are modelled by harmonic oscillator functions. This results in the expression:

$$V_{22}(r_{NH}, Q_c) = \frac{1}{2}(v_{21}(r_{NH}) + v_{22}(r_{NH})) - \frac{1}{2}\sqrt{[v_{21}(r_{NH}) - v_{22}(r_{NH})]^2 + 4\lambda_{22}^2} \quad + \sum_c \frac{1}{2}\omega_c^{(2)}(r_{NH})Q_c^2, \tag{A.3}$$

where

$$v_{21}(r_{NH}) = D_e^{21}[1 - \exp(-a_{21}(r_{NH} - r_{21}))]^2 + E_0^2, \tag{A.4}$$

$$v_{22}(r_{NH}) = A_{22}\exp(-a_{22}(r_{NH} - r_{22})) + D_e^{22}, \tag{A.5}$$

and D_e^{22} corresponds to the dissociation energy of the diabatic $^1\pi\sigma^*$ state.

The coupling element in the diabatic representation is approximately by a linear function:

$$V_{12} = \sum_c \lambda_c(r_{NH})Q_c. \tag{A.6}$$

The detailed procedure of obtaining the parameters in the above equations via the fitting of adiabatic *ab initio* data has been described in the previous papers [10,11]. Here we just outline the basic idea. First, we put all $Q_c = 0$ in this model and obtain the parameters related to v_{11}, v_{21} and v_{22} by a non-linear fitting using the *ab initio* data of the 1D cut of the PE functions along r_{NH}. One-dimensional adiabatic PE curves are calculated for each of the coupling modes for different NH distances. This yields $\omega_c^{(1)}$, $\omega_c^{(2)}$ and λ_c as functions of r_{NH}. Finally, we have chosen appropriate analytic functions to fit the r_{NH} dependence of these parameters.

For the $^1A_2$– S_0 conical intersection, Q_{11} is the strongest coupling mode, while Q_{10} and Q_{12} are weak coupling modes. It is found that the diabatic frequencies for all these modes do not depend on r_{NH}.

We choose the following expression for the dependence of the diabatic coupling strength λ_c on r_{NH}:

$$\lambda_c(r_{NH}) = \frac{1}{2}\lambda_{12}^{max}\left[1 - \tanh\left(\frac{r_{NH} - d_{12}}{\beta_{12}}\right)\right] + \lambda_0. \tag{A.7}$$

Tables A.1 and A.2 give the values of the parameters of the diabatic model defined by Eqs. (A.1)–(A.7). The average deviation between the fit and the *ab initio* data is 0.01 eV, reaching a maximum of 0.05 eV in the region of the barrier in the $^1\pi\sigma^*$ state.

Table A.1
Values of the parameters for v_{11}, v_{21} and v_{22} for the $^1A_2$– S_0 model

V_{11}	V_{22}	
v_{11}	v_{21}	v_{22}
$D_e^1 = 4.979$ eV	$E_0^2 = 4.805$ eV	$A_{22} = 2.644$ eV
$r_1 = 1.927$ au	$D_e^{21} = 4.979$ eV	$D_e^{22} = 3.956$ eV
$a_1 = 1.137$ au	$r_{21} = 1.882$ au	$r_{22} = 2.216$ au
	$a_{21} = 1.293$ au	$a_{22} = 1.325$ au
	$\lambda_{22} = 1.248$ eV	

Table A.2
Values of the parameters pertaining to the coupling modes for the $^1A_2$– S_0 model

ω	λ
Q_{10}	
$\omega_c = 0.1022$ eV	$\lambda_{12}^{max} = 0.066$ eV
$\omega_c^{(1)} = 0.1077$ eV	$d_{12} = 4.364$ au
$\omega_c^{(2)} = 0.1155$ eV	$\beta_{12} = 1.478$ au
	$\lambda_0 = 0$ au
Q_{11}	
$\omega_c = 0.0825$ eV	$\lambda_{12}^{max} = 0.237$ eV
$\omega_c^{(1)} = 0.1096$ eV	$d_{12} = 3.679$ au
$\omega_c^{(2)} = 0.1096$ eV	$\beta_{12} = 1.369$ au
	$\lambda_0 = 0$ au
Q_{12}	
$\omega_c = 0.0756$ eV	$\lambda_{12}^{max} = 0.151$ eV
$\omega_c^{(1)} = 0.0887$ eV	$d_{12} = 2.643$ au
$\omega_c^{(2)} = 0.0487$ eV	$\beta_{12} = 0.980$ au
	$\lambda_0 = 0.021767$ au

Table A.3
Values of the parameters for v_{11}, v_{21} and v_{22} for the $^1B_1$– S_0 model

V_{11}	V_{22}	
v_{11}	v_{21}	v_{22}
$D_e^1 = 5.117$ eV	$E_0^2 = 5.584$ eV	$A_{22} = 0.091$ eV
$r_1 = 1.959$ au	$D_e^{21} = 8.070$ eV	$D_e^{22} = 4.092$ eV
$a_1 = 1.196$ au	$r_{21} = 1.922$ au	$r_{22} = 5.203$ au
	$a_{21} = 0.822$ au	$a_{22} = 1.290$ au
	$\lambda_{22} = 1.669$ eV	

For the $^1B_1$– S_0 conical intersection, Q_{24} is the strong coupling mode and Q_{22} also couples these two states with medium strength, while the coupling by Q_{21} and Q_{23} is close to zero. Thus it is reasonable to neglect Q_{21} and Q_{23} in this model. For Q_{22} and Q_{24}, the dependence of the diabatic coupling strength on r_{NH} is described by Eq. (A.7). It is found that the diabatic frequencies $\omega_c^{(1)}$ and $\omega_c^{(2)}$ do not depend on r_{NH} for Q_{22}. The diabatic frequencies $\omega_c^{(1)}$ and $\omega_c^{(2)}$ of Q_{24}, on the other hand, decrease with increasing NH coordinate. We have used the following function to represent the diabatic frequencies of Q_{24} as functions of r_{NH}:

$$\omega_c^{(i)}(r_{NH}) = \frac{1}{2}a_i\left[1 - \tanh\left(\frac{r_{NH} - b_1}{c_i}\right)\right] + d_i. \tag{A.8}$$

Tables A.3 and A.4 give the values of all parameters of the $^1B_1$– S_0 model. Due to the very small contribution of ν_{21} and ν_{23} to the diabatic coupling element, they are not included in the tables. The average deviation between the fit and the *ab initio* data is 0.015 eV.

Appendix B. Preparations of the initial states

In the MGBR approach, the 3D WP is expressed as

$$|\Psi(t)\rangle = \int dr \sum_{i,m,n} \chi_{i,m,n}(r, t)\langle r|\langle n|\langle m|\langle\phi_i^e|\Psi(t)\rangle. \tag{B.1}$$

Table A.4
Values of the parameters pertaining to the coupling modes for the $^1B_1$– S_0 model

ω		λ
Q_{22}		
ω_c	$\omega_c = 0.0888$ eV	$\lambda_{12}^{\max} = 0.0738$ eV
$\omega_c^{(1)}$	$\omega_c^{(1)} = 0.0650$ eV	$d_{12} = 4.0728$ au
$\omega_c^{(2)}$	$\omega_c^{(2)} = 0.1260$ eV	$\beta_{12} = 0.0910$ au
		$\lambda_0 = 0.0$ au
Q_{24}		
ω_c	$\omega_c = 0.0640$ eV	$\lambda_{12}^{\max} = 0.4269$ eV
$\omega_c^{(1)}$	$a_1 = 0.0718$ eV	$d_{12} = 4.8319$ au
	$b_1 = 2.5805$ au	$\beta_{12} = 1.3225$ au
	$c_1 = 1.4619$ au	$\lambda_0 = 0.0$ au
	$d_1 = 0.0753$ au	
$\omega_c^{(2)}$	$a_2 = 0.0718$ eV	
	$b_2 = 2.5805$ au	
	$c_2 = 1.4619$ au	
	$d_2 = 0.0143$ au	

Here, the WP is given in the coordinate-space representation for the NH stretching coordinate r. For the coupling modes, on the other hand, the WP is expressed in basis functions, $|n\rangle$ and $|m\rangle$, which represent sets of harmonic oscillator functions for the two coupling modes. The $|\phi_i^{\mathrm{e}}\rangle$ are diabatic or adiabatic electronic states. In this representation, the time-dependent nuclear WP on the ith diabatic or adiabatic electronic state as $\chi_{i,m,n}^{\mathrm{d}}(r,t)$ or $\chi_{i,m,n}^{\mathrm{a}}(r,t)$, respectively.

To define the initial preparation of the system, we first generate the vibrational eigenstates of the adiabatic electronic ground-state PE surface V_1^{a}. The Hamiltonian for the electronic ground state is

$$H_{\mathrm{ground}} = T + V_1^{\mathrm{a}} = \frac{\hbar^2}{2\mu}\frac{\partial^2}{\partial r^2} - \sum_c \frac{1}{2}\omega_c \frac{\partial^2}{\partial Q_c^2} + V_1^{\mathrm{a}}(r, Q_c, \ldots). \tag{B.2}$$

After the separation of the Hamiltonian into three parts,

$$H_{\mathrm{ground}} = H_1 + H_2 + H_3, \qquad H_1 = -\frac{\hbar^2}{2\mu}\frac{\partial^2}{\partial r^2},$$

$$H_2 = \sum_c \frac{1}{2}\omega_c \left(-\frac{\partial^2}{\partial Q_c^2} + Q_c^2\right),$$

$$H_3 = V_1^{\mathrm{a}}(r, Q_c, \ldots) - \sum_c \frac{1}{2}\omega_c Q_c^2. \tag{B.3}$$

it is straightforward to represent each of them with the help of the discrete variable representation (DVR) and finite variable representation (FBR). The kinetic operator H_1 of the r part is represented by the Colbert-Miller DVR [36], which is essentially the Fourier basis. The matrix element of H_2 can be evaluated directly with harmonic-oscillator basis functions. The residual Hamiltonian H_3 only depends on the coordinates. Its matrix elements also be evaluated efficiently with the FBR/DVR method.

The concept of the FBR/DVR method has been discussed by many authors (see Ref. [37] for a review). Here, we adopt a rather simple approach as follows [38]. In the coordinate space, the DVR grid points for the coupling modes are calculated by diagonalization of the coordinate operator $\hat{Q}$ in the given harmonic-oscillator basis set

$$\langle n_1|\hat{Q}_c|n_2\rangle = \sum_{Q_c} \langle n_1|Q_c\rangle Q_c \langle Q_c|n_2\rangle. \tag{B.4}$$

The set of eigenvalues Q_c of $\hat{Q}_c$ provides the local grid points and the corresponding eigenvectors $\langle Q_c|n_i\rangle$ define the transformation matrix between basis and grid. Labelling two coupling modes as $Q_{c,1}$ and $Q_{c,2}$, matrix elements of H_3 can be evaluated as:

$$\begin{aligned}&\langle r_1, n_1, m_1|H_3|r_2, n_2, m_2\rangle \\ &= \sum_{Q_{c,1}, Q_{c,2}} \langle n_1|Q_{c,1}\rangle\langle m_1|Q_{c,2}\rangle H_3(r_1, Q_{c,1}, Q_{c,2})\langle Q_{c,1}|n_2\rangle \\ &\quad \times \langle Q_{c,2}|m_2\rangle\delta_{r_1,r_2}.\end{aligned} \tag{B.5}$$

For the r coordinate, we have employed 64 DVR points from 3.0 to 6.2 au. We have used 10 harmonic-oscillator basis functions to represent the Hamiltonian for the two coupling modes.

For the kth vibrational state $\chi_{1,k}^{(\mathrm{a})}$ of the adiabatic ground electronic state $|\phi_1^{(\mathrm{a})}\rangle$, the total wavefunction Ψ_0 in the adiabatic representation can be written as

$$|\Psi_0\rangle = \chi_{1,k}^{(\mathrm{a})}|\phi_1^{(\mathrm{a})}\rangle. \tag{B.6}$$

The initial WP is prepared by vertical excitation of $|\Psi_0\rangle$ to the adiabatic excited state $|\phi_2^{(\mathrm{a})}\rangle$. Employing the unitary transformation matrix $\mathbf{U}$ of Eq. (1), we obtain the initial nuclear WP $\chi^{(\mathrm{d})}(t=0)$ in the diabatic representation for the propagation. Because the WPs are expressed in the MGBR and the transformation matrix $\mathbf{U}$ depends on the nuclear coordinates $(r, Q_{c,1}, Q_{c,2})$, The FBR/DVR technique is employed to perform this adiabatic-to-diabatic transformation.

Appendix C. Details of the WP propagation

The WPs are propagated in the MGBR (see Appendix B) on the two coupled surfaces using the split-operator (SO) method [39]. We employ the fast Fourier transform (FFT) method [40] to evaluate the kinetic-energy operator of the r coordinate. We use the same grid spacing here and extend our grid to 256 points, from 3.0 to 15.8 au. Ten harmonic-oscillator basis functions are employed for each of the coupling modes. The wave packets are propagated for 200 fs for the $^1B_1$– S_0 and $^1A_2$– S_0 conical intersections, respectively, with a time step of 0.1 fs. All calculations have been checked to guarantee converged results with respect to grid size and time step.

The dissociation probability on the ith diabatic electronic state is defined as the time-accumulated flux through a dividing surface located at $r = r_{\mathrm{flux}}$ in the asymptotic region [21,41]

$$F_i^{\mathrm{D}}(t) = \frac{\hbar}{\mu}\int_{t=0}^{t} \mathrm{Im}\left[\left\langle \chi_{i,m,n}^{(\mathrm{d})}(r,t)\middle|\frac{\partial \chi_{i,m,n}^{(\mathrm{d})}(r,t)}{\partial r}\right\rangle\right]\Bigg|_{r=r_{\mathrm{flux}}} \mathrm{d}t. \tag{C.1}$$

To avoid reflection at the grid boundary in the r direction, we apply a damping function [41],

$$f(r) = \sin\left[\frac{\pi}{2}\frac{(r_{\mathrm{mask}} + \Delta r_{\mathrm{mask}} - r)}{\Delta r_{\mathrm{mask}}}\right], \quad r_{\mathrm{mask}} < r < r_{\mathrm{max}} \tag{C.2}$$

between $r_{\mathrm{mask}} = 13.5$ au and $r_{\mathrm{max}} = 15.8$ au to remove the dissociative WP.

The diabatic electronic population probabilities are calculated as follows. Instead of using the large grid for the stretching coordinate r, we put a surface at $r_{\mathrm{D}} = 13.5$ au in the asymptotic region of the potential surface to measure the dissociation flux. Then we define the diabatic electronic population probability as the sum of the probability of the nuclear WP in the region of $[0, r_{\mathrm{D}}]$ and the flux penetrating the surface at r_{D}:

$$P_i^{\mathrm{d}}(t) = \int_0^{r_{\mathrm{D}}} \sum_{n,m} |\chi_{i,m,n}^{(\mathrm{d})}(r,t)|^2 \,\mathrm{d}r + F_i^{\mathrm{D}}(t). \tag{C.3}$$

To determine the adiabatic populations, we use a similar technique:

$$P_i^{\mathrm{a}}(t) = \int_0^{r_{\mathrm{D}}} \sum_{n,m} |\chi_{i,m,n}^{(\mathrm{a})}(r,t)|^2 \,\mathrm{d}r + F_i^{\mathrm{D}}(t). \tag{C.4}$$

The transformation between $\chi_{i,m,n}^{(\mathrm{a})}(r,t)$ and $\chi_{i,m,n}^{(\mathrm{d})}(r,t)$ is again evaluated using FBR/DVR methods.

References

[1] M.H. Palmer, I.C. Walker, M.F. Guest, Chem. Phys. 238 (1998) 179.
[2] O. Christiansen, J. Gauss, J.F. Stanton, P. Jørgensen, J. Chem. Phys. 111 (1999) 525.
[3] B.O. Roos, P.-A. Malmqvist, V. Molina, L. Serrano-Andrés, M. Merchán, J. Chem. Phys. 116 (2002) 7526.
[4] A.L. Sobolewski, W. Domcke, C. Dedonder-Lardeux, C. Jouvet, Phys. Chem. Chem. Phys. 4 (2002) 1093.
[5] P. Celani, H.-J. Werner, J. Chem. Phys. 119 (2003) 5044.
[6] D.A. Blank, S.W. North, Y.T. Lee, Chem. Phys. 187 (1994) 35.
[7] J. Wei, A. Kuczmann, J. Riedel, F. Renth, F. Temps, Phys. Chem. Chem. Phys. 5 (2004) 315.
[8] J. Wei, J. Riedel, A. Kuczmann, F. Renth, F. Temps, Faraday Discuss. 127 (2004) 267.
[9] H. Lippert, H.H. Ritze, I.V. Hertel, W. Radloff, ChemPhysChem 5 (2004) 1423.
[10] V. Vallet, Z. Lan, S. Mahapatra, A.L. Sobolewski, W. Domcke, Faraday Discuss. 127 (2004) 283.
[11] V. Vallet, Z. Lan, S. Mahapatra, A.L. Sobolewski, W. Domcke, J. Chem. Phys 123 (2005) 144307.
[12] H. Köppel, E.V. Gromov, A.B. Trofimov, Chem. Phys. 304 (2004) 35.
[13] B. Cronin, M.G.D. Nix, R.H. Qadiri, M.N.R. Ashfold, Phys. Chem. Chem. Phys. 6 (2004) 5031.
[14] B. Cronin, A.L. Devine, M.G.D. Nix, M.N.R. Ashfold, Phys. Chem. Chem. Phys. 8 (2006) 3440.
[15] B. Cronin, M.G.D. Nix, A.L. Devine, R.N. Dixon, M.N.R. Ashfold, Phys. Chem. Chem. Phys. 8 (2006) 599.
[16] M.N.R. Ashfold, B. Cronin, A.L. Devine, M.G.D. Nix, Science 312 (2006) 1637.
[17] H. Köppel, W. Domcke, L.S. Cederbaum, Adv. Chem. Phys. 57 (1984) 59.
[18] T.H. Dunning, J. Chem. Phys. 90 (1989) 1007.
[19] M.J. Frisch, et al., GAUSSIAN 98, Gaussian, Inc., Pittsburgh, PA, 2000.
[20] MOLPRO is a package of ab initio programs written by H.-J. Werner, P.J. Knowles, with contributions from R.D. Amos, A. Berning, D.L. Cooper, M.J.O. Deegan, A.J. Dobbyn, F. Eckert, C. Hampel, G. Hetzer, T. Leininger, R. Lindh, A.W. Lloyd, W. Meyer, M.E. Mura, A. Nicklaß, P. Palmieri, K. Peterson, R. Pitzer, P. Pulay, G. Rauhut, M. Schütz, H. Stoll, A.J. Stone, T. Thorsteinsson.
[21] W. Domcke, D.R. Yarkony, H. Köppel, Conical Intersections: Electronic Structure, Dynamics and Spectroscopy, World Scientific, Singapore, 2004.
[22] V. Sidis, Adv. Chem. Phys. 82 (1992) 73.
[23] T. Pacher, L.S. Cederbaum, H. Köppel, Adv. Chem. Phys. 84 (1993) 293.
[24] A.J. Gianola, T. Ichino, R.L. Hoenigman, S. Kato, V.M. Bierbaum, W.C. Lineberger, J. Phys. Chem. 108 (2004) 10326.
[25] A. Motzke, Z. Lan, C. Woywod, W. Domcke, Chem. Phys. 329 (2006) 50.
[26] L.S. Cederbaum, E. Gindensperger, I. Burghardt, Phys. Rev. Lett. 94 (2005) 113003.
[27] E. Gindensperger, I. Burghardt, L.S. Cederbaum, J. Chem. Phys. 124 (2006) 144103.
[28] E. Gindensperger, I. Burghardt, L.S. Cederbaum, J. Chem. Phys. 124 (2006) 144104.
[29] H. Nakatsuji, O. Kitao, T. Yonezawa, J. Chem. Phys. 83 (1985) 723.
[30] H. Nakano, T. Tsuneda, T. Hashimoto, K. Hirao, J. Chem. Phys. 104 (1996) 2312.
[31] K.R.F. Somers, E.S. Kryachko, A. Ceulemans, J. Phys. Chem. A. 107 (2003) 5427.
[32] R. Burcl, S. Carter, N.C. Handy, Phys. Chem. Chem. Phys. 6 (2004) 340.
[33] A. Bach, J.M. Hutchison, R.J. Holiday, F.F. Crim, J. Phys. Chem. 107 (2003) 10490.
[34] M.L. Hause, Y.H. Yoon, F.F. Crim, J. Chem. Phys. 125 (2006) 174309.
[35] M. Barbatti, M. Vazdar, A.J.A. Aquino, M. Eckert-Maksić, H. Lischka, J. Chem. Phys. 125 (2006) 164323.
[36] D.T. Colbert, W.H. Miller, J. Chem. Phys. 96 (1992) 1.
[37] J.C. Light, T. Carrington Jr., Adv. Chem. Phys. 114 (2000) 263.
[38] U. Manthe, H. Köppel, J. Chem. Phys. 93 (1990) 345.
[39] D. Feit, J.A. Fleck, A. Steiger, J. Comput. Phys. 47 (1982) 412.
[40] D. Kosloff, R.A. Kosloff, J. Comput. Phys. 52 (1983) 35.
[41] S. Mahapatra, N. Sathyamurthy, J. Chem. Soc., Faraday Trans. 97 (1997) 9062.